Materials & Design 249 (2025) 113547

Contents lists available at ScienceDirect

Materials & Design

journal homepage: www.elsevier.com/locate/matdes

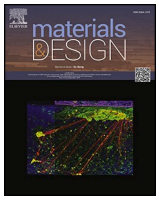

Precipitation 3D printing of all-aramid materials for high-strength, heat-resistant applications

Ruowen Tu [a,d], Hyun Chan Kim [b,*], Henry A. Sodano [a,c]

[a] Department of Aerospace Engineering, University of Michigan, Ann Arbor, MI 48109, USA
[b] Department of Mechanical System Engineering, Kumoh National Institute of Technology, Gumi, Gyeongbuk 39177, Republic of Korea
[c] Department of Macromolecular Science and Engineering, University of Michigan, Ann Arbor, MI 48109, USA
[d] Bioinspired Soft Robotics Laboratory, Istituto Italiano di Tecnologia, Genova 16163, Italy

ARTICLE INFO

Keywords:
Aramid nanofiber
Self-assembly
Additive manufacturing
Precipitation printing
High-temperature

ABSTRACT

Additive manufacturing (AM) of lightweight, high-performance engineering polymers is an important research focus in the automotive, electronics and aerospace industries. Aramid material is a highly crystalline polymer in the form of fibers with superior mechanical and thermal properties than most high-performance thermoplastics used in AM. However, manufacturing all-aramid 3D structures has been challenging due to the processing difficulty of aramid. In this work, AM of all-aramid 3D structures is achieved by two approaches: simultaneous protonation and precipitation printing of aramid nanofiber (ANF) colloids, and precipitation printing of aramid/sulfuric acid liquid crystalline solutions. After comparison, the ANF approach proves superior to the sulfuric acid method, offering enhanced printability, greater mechanical strength in the printed parts, and improved capability for microstructure customization. Specifically, the dense all-aramid structures produced through the ANF approach exhibit exceptional mechanical properties, with a Young's modulus of 7.2 GPa and a tensile strength of 146.6 MPa, outperforming other unfilled, high-performance polymers manufactured through AM. These structures are also capable of withstanding extreme environments, including temperatures up to 350 °C. Therefore, high-performance all-aramid 3D structures can be realized via ANF-based precipitation 3D printing, which can be used as lightweight structural or heat protection parts in aircraft and automotive systems.

1. Introduction

High-performance engineering polymers are a class of polymers known for their superior thermal stability and mechanical properties especially when exposed to elevated temperatures, setting them apart from standard engineering polymers. This class of polymers typically possesses a high decomposition temperature (T_d) above 450 °C, excellent chemical resistance, and good long-term mechanical performance at 177 °C. Thanks to these attributes, high-performance polymers are widely used in industries such as electronics, energy, transportation, aerospace and defense [1,2]. Despite their numerous advantages, high-performance polymers are often produced in small quantities. This is due to their specialized applications and higher production costs compared to standard engineering polymers. In this context, additive manufacturing (AM), also known as 3D printing, is an ideal manufacturing process for high-performance polymers. AM offers significant processing advantages, including design freedom, scalability and material efficiency. Additionally, for low-volume production, AM is more cost-efficient than traditional injection molding [1,3,4].

Currently, notable high-performance thermoplastics tailored for AM processes include the following materials: the amorphous polysulfone family (PSUs) with a glass transition temperature (T_g) ranging from 185 to 220 °C [5], amorphous polyetherimide (PEI) with a T_g of 217 °C [6], and the semi-crystalline polyaryletherketone family (PAEKs) with a T_g spanning from 147 to 164 °C and a melting temperature T_m between 343 to 372 °C [7–9]. Additionally, both amorphous and semi-crystalline thermoplastic polyimide (TPI) with a T_g of 249 °C are included in this category, which has the highest heat resistance among all commercially available thermoplastics for AM [10]. The amorphous PSUs and PEI have been successfully manufactured in a filament form for material extrusion, necessitating a nozzle temperature at least 150 °C above their T_g for continuous extrusion [11–13]. The AM of semi-crystalline PAEKs can be achieved either through material extrusion of PAEK filaments, which requires a nozzle temperature approximately 40 °C above their

* Corresponding author.
E-mail address: hyunckim@kumoh.ac.kr (H.C. Kim).

https://doi.org/10.1016/j.matdes.2024.113547
Received 5 November 2024; Received in revised form 6 December 2024; Accepted 13 December 2024
Available online 18 December 2024

T_m [9,14–16] or through powder bed fusion of fine PAEK powders [17,18]. For TPI, its remarkable thermal resistance demands extremely high nozzle temperature for material extrusion, potentially leading to weakened interfacial bonding between deposited paths due to significant temperature gradients [19]. To improve printability for material extrusion, polymer blending of amorphous and semi-crystalline high-performance thermoplastics is an alternative approach. Literature showed that polyether ether ketone (PEEK) and PEI can form miscible polymer blends regardless of the composition [20]. Thus, multiple research groups developed PEEK/PEI blends for material extrusion [21,22], which could be used for potential aerospace applications. Moreover, material extrusion of high-performance thermoplastics allows for the incorporation of filler reinforcements, including nanofillers [23,24], short fibers [22,25] and continuous fibers [12,26], to further strengthen the printed parts. In addition to high-performance thermoplastics, research has also explored AM of thermosetting polyimides (PI). This has been approached by synthesizing photocurable precursors for vat photopolymerization or ultraviolet-assisted direct ink writing (DIW) [27–30]. High molecular weight PI has also been synthesized as filaments for the material extrusion process by Abbott et al. [31]. All printed green parts were then imidized by heating them above 240 °C, resulting in crosslinked PI structures with exceptional mechanical and thermal properties.

Para-aramid (poly-*p*-phenylene terephthalamide) fiber, often recognized by the brand name Kevlar®, exhibits superior heat resistance and mechanical properties when compared to most of the high-performance polymers mentioned above. This is due to its rigid aromatic backbone, high degree of crystallinity, and strong hydrogen bonding between aramid chains. Most *para*-aramid fibers show weak glass transition behavior (T_g around 330 °C) because of their high crystallinity, and they typically decompose (T_d above 500 °C) before melting [8,32]. However, they are only available in the form of fibers due to the solution spinning process, which prevents them from being melt extruded or injection molded, thus restricting the production of bulk all-aramid 3D structures. In the last decade, the development of a dissolution and deprotonation process to prepare aramid nanofiber (ANF) colloids through the disassembly of macroscale *para*-aramid fibers using dimethyl sulfoxide (DMSO) and alkali bases like potassium hydroxide (KOH) provided a nanoscale building block for all-aramid structures [33,34]. Colloidal self-assembly of ANFs into macroscale filaments [35], films [36–38], and nano papers [39–41] have been successfully developed as a scalable approach to fabricate 1D and 2D structures that inherit the outstanding thermal and mechanical properties of *para*-aramid fibers. Research on AM of ANF-based 3D structures has also been explored. DIW of DMSO-based ANF inks on a cold substrate has been used to form 3D ANF cryogels, which can be post-processed into 3D aerogels by freeze-drying [42]. However, AM of nonporous all-aramid 3D structures has not yet been achieved. Further advancements in this field could facilitate significant progress towards the fabrication of high-performance, all-aramid 3D structures.

Precipitation 3D printing, or simply precipitation printing, is a solution-based AM process inspired by wet spinning, where a solvated polymer is extruded into a non-solvent coagulation bath following the designed tool paths, and precipitates as a solid structure. While previous research on precipitation printing has primarily focused on thermoplastic/solvent solutions [43–45], extending precipitation printing to other types of liquid mixtures as the printing ink remains largely unexplored. In this paper, two precipitation printing-based approaches are developed for the AM of all-aramid 3D structures: an ANF approach using ANF colloids and a sulfuric acid (H_2SO_4) approach using aramid/H_2SO_4 liquid crystalline solutions. In both approaches, the printing ink is precipitation printed into a non-solvent coagulation bath, where the aramid either protonates or precipitates to form solid but wet structures. The wet structures are then washed and dried to produce final structures through either thermal drying or freeze-drying. After comparing the printability, crystallinity, microstructure morphology, mechanical properties, and thermal properties of the all-aramid parts fabricated through the two approaches, the ANF approach is selected as a more reliable and effective process to produce high-quality all-aramid 3D structures.

2. Experimental section

2.1. Preparation of printing inks

For the ANF approach, the printing inks were prepared based on the extensively studied aramid fabric deprotonation and dissolution process to form ANFs colloids [33,46,47]. Six high-concentration ANF printing inks (colloids) with different compositions (Table 1) were prepared for the precipitation printing process. To prepare each ANF printing ink, *para*-aramid fabrics (Kevlar® KM2+, style 790, CS-800) were cut into small pieces, disintegrated into fiber bundles and weighed inside a 250 mL glass bottle to obtain the corresponding amount in Table 1. The amount of KOH (Fisher Chemical) was weighed in a small beaker and deionized (DI) water was then added to the beaker to dissolve KOH, according to Table 1. The resulting high-concentration KOH aqueous solution was poured into the bottle with already weighed fabrics, followed by adding the designed amount of DMSO (certified ACS, Sigma Aldrich) to the same bottle. It should be noted that instead of using the original KOH/DMSO system to dissolve aramid fabric [33], the addition of DI water in this system is to increase the solubility of KOH in the solution and prepare high-concentration ANF printing inks [47]. For all ANF printing inks, the amount of DI water was kept as 4 wt% of DMSO for the fastest dissolution, following the results by Yang et al. [47]. The resulting aramid/KOH/DMSO/water mixture was poured into a 500 mL Teflon® liner installed in a pressure reactor (Parr 4560 series) with a turbine type impeller, heated at 60 °C and stirred at 200 RPM for a day (Fig. S1). The deprotonation and dissolution process at 60 °C could decrease aramid intermolecular bonding, reduce colloid viscosity and induce some amide hydrolysis due to the presence of water [48,49], which improved the saturation concentration of ANFs in the colloids. After mixing, a highly viscous but homogeneous ANF colloid with a dark red color could be obtained.

For the sulfuric acid approach, the printing ink was prepared by dissolving aramid into high concentration H_2SO_4 to form a liquid crystalline solution, which was adopted from the industrial manufacturing process for spinning aramid fibers. In this work, aramid fabrics (Kevlar® KM2+, style 790, CS-800) were cut into small pieces and dissolved in high concentration (>98 %) H_2SO_4 (Certified ACS Plus, Fisher Chemical) to form a 10 wt% liquid crystalline solution in a glass bottle, which was mixed via magnetic stirring and sonication for 7 days. It should be noted that the 10 wt% concentration was selected as the highest concentration achieved by the lab-scale mixing device to maximize printing efficiency.

2.2. Precipitation printing through the ANF approach

The printing process for all-aramid structures through the ANF approach was a combination of the simultaneous wet spinning and protonation process to produce tough ANF-assembled filaments

Table 1
Composition of the six ANF printing inks used in this work.

ANF printing ink	Ink 1	Ink 2	Ink 3	Ink 4	Ink 5	Ink 6
Aramid fabric (g)	7.5	12	12.5	12.5	14	16.1
KOH (g)	3.75	5.3	4	4.63	5.6	6
DMSO (g)	150	200	150	150	150	150
DI water (g)	6	8	6	6	6	6
KOH/aramid ratio	50 %	44 %	32 %	37 %	40 %	37 %
Measured ANF concentration (wt%)	4.5	6.3	7.2	7.2	8.8	9.7

previously developed by our group [35], and the computer-controlled precipitation printing process [43,44]. The top row of Fig. 1A summarizes the whole fabrication process for all-aramid materials through the ANF approach. After preparing the ANF printing inks, the inks were loaded in a 10 mL polypropylene syringe with a 0.84 mm diameter stainless-steel nozzle. Fig. 1B shows the precipitation printing setup, where the syringe was controlled by a precision dispenser (Ultimus V, Nordson EFD) and a gantry system (AGS1500, Aerotech) using G-code. The non-solvent coagulation bath for the ANF approach was propylene glycol (PG, 99.9 %, SK picglobal), a weak proton donor for the ANF protonation process. PG was selected as the coagulation bath from the common weak proton donors listed in Table S1, due to its high viscosity, which enables slow solvent diffusion, its high boiling point, which minimizes evaporation loss, and its low toxicity. A piece of 120 grit sandpaper with adhesive backing was attached to a glass plate and then immersed in the non-solvent bath to act as the printing substrate. The highly rough abrasive particles on the sandpaper could create physical entanglements with the extruded first-layer printing ink, allowing for a physical bonding of the print to the substrate (Fig. S2). For all prints, the layer height was 0.25 mm, the printing width was set the same as the nozzle diameter, and the printing speed was 14 mm·s^{-1} for the ANF approach. The printing pressure was adjusted for different printing inks to achieve maximum infill. The tool paths were generated by slicing 3D structures in STL files using Cura, and three infill patterns, all 0°, all 90° and 0°/90° alternating, were used for mechanical testing. After precipitation printing, the sample was removed from the sandpaper by a metal spatula, and the sandpaper could be reused for multiple times if the gaps between the abrasive particles were cleaned by a sharp tip or a brush.

The detailed precipitation printing mechanism through the ANF approach is shown in Fig. 1C. When the ANF printing ink is extruded out of the syringe nozzle that is immersed in the PG coagulation bath, the DMSO and KOH in the ANF printing ink slowly diffuse into the PG bath, which results in simultaneous protonation and precipitation of the ANFs, as well as a color change from dark red to yellow. After printing, the printed wet ANF structures were removed from the PG coagulation bath and immersed in a DI water bath for 2–3 h to wash away the residual solvents and KOH, which was repeated 3 times with fresh DI water. After washing, dense all-aramid structures produced through the ANF approach (termed dense A-aramid, sample names summarized in Table S2) can be obtained through thermal drying which involves 50 °C drying for 12 h and 300 °C post-heating for 1 h in a convection oven, while porous all-aramid structures produced through the ANF approach (termed porous A-aramid) can be formed through freeze drying which requires − 20 °C freezing for 1 day in a freezer and vacuum drying using a freeze drier (FreeZone, Labconco).

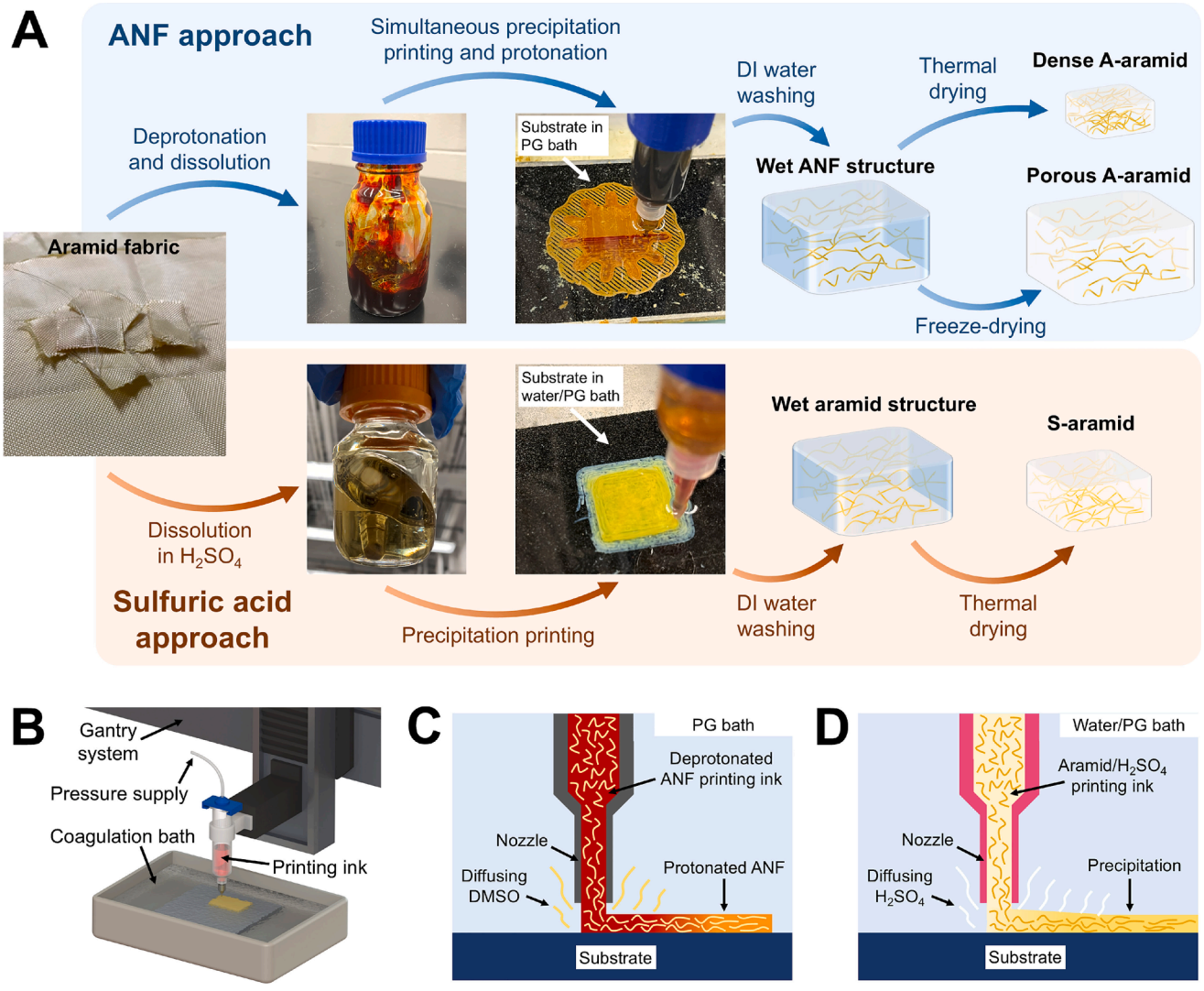

Fig. 1. A) Flowchart of the additive manufacturing processes of all-aramid materials through the ANF approach and sulfuric acid approach. B) Precipitation printing setup. C) Printing mechanism illustration of the ANF approach. D) Printing mechanism illustration of the sulfuric acid approach.

2.3. Precipitation printing through the sulfuric acid approach

The precipitation printing process for all-aramid structures through the sulfuric acid approach was designed based on the industrial solution spinning process for the manufacturing of aramid fibers [50]. As shown in the fabrication flow chart in the bottom row of Fig. 1A, after preparing the aramid/H_2SO_4 liquid crystalline printing ink, the ink was then loaded in a syringe with a 0.60 mm diameter polypropylene nozzle. In this case, the coagulation bath for precipitation printing was a water/PG (50:50 vol%) mixture, which was selected by balancing the precipitation rate and interlayer bonding performance. The printing speed was 6 mm·s^{-1} for the sulfuric acid approach, slower than the ANF approach, because of the slower diffusion rate of the viscous aramid/H_2SO_4 printing ink into the coagulation bath. The printing pressure was adjusted to achieve maximum infill. All other printing setups and parameters for the sulfuric acid approach were kept the same as the ANF approach. Fig. 1D illustrates the printing mechanism of the sulfuric acid approach, where the transparent aramid/H_2SO_4 printing ink is extruded into the water/PG bath. The H_2SO_4 slowly diffuses into the water/PG bath, which results in the precipitation of yellow aramid on the printing substrate to form wet aramid structures. The printed wet aramid structures were removed from the sandpaper substrate and immersed in a DI water bath for 2–3 h to wash away the residual PG and H_2SO_4, which was repeated 4–5 times with fresh DI water. After thermal drying at 50 °C for 12 h and post-heating at 300 °C for 1 h in a convection oven, the wet aramid structures turned into S-aramid (sample names summarized in Table S2) structures.

2.4. Characterization methods

The viscosity of the ANF printing inks was measured using a cone-plate viscometer (DVNext, AMETEK Brookfield) at room temperature, under a shear rate between 0.075 to 15 s^{-1}. The morphology and diameter of protonated and isolated ANFs from different ANF printing inks were characterized using an atomic force microscope (AFM, XE-70, Park Systems). Fourier-transform infrared spectroscopy (FTIR) and X-ray diffraction (XRD) were performed on printed all-aramid samples using a Nicolet is50 spectrometer with Smart iTR attenuated total reflectance accessory (Thermo Scientific) and an Ultima IV diffractometer (Rigaku) with a CuKα radiation source ($\lambda = 0.154$ nm), respectively. Scanning electron microscopy (SEM) images of the cross-sections of the all-aramid samples were taken from a JSM-7800FLV microscope (JEOL).

2.5. Mechanical and thermal testing methods

The mechanical properties of the printed all-aramid specimens were characterized through tensile testing following ASTM D638, where specimens were designed to have the type V specimen shape after drying by considering the contraction ratio. All tensile tests were performed on an Instron E3000 testing frame with an extension rate of 1 mm·min^{-1}. For thermal properties, thermogravimetric analysis (TGA, Q600, TA Instruments) was performed on the all-aramid samples from 30 to 1000 °C with a rate of 10 °C·min^{-1} in nitrogen, and tensile mode dynamic mechanical analysis (DMA, Q800, TA Instruments) was measured at 1 Hz frequency from 30 to 500 °C with a rate of 5 °C·min^{-1} in air.

3. Results

3.1. Precipitation printing of All-Aramid 3D structures

In this research, two approaches are proposed for the AM of all-aramid materials: the ANF approach and the sulfuric acid approach. For the ANF approach, preparing high-concentration ANF colloids as printing inks is a crucial foundation for the efficient fabrication of all-aramid materials. Here, six different ANF printing inks (Table 1) were prepared by adding 4 wt% water relative to DMSO into the typical aramid/KOH/DMSO system to increase the solubility of KOH [47] together with an elevated temperature mechanical stirring for aramid dissolution. The resulting printing inks have measured ANF concentrations ranging from 4.5 wt% to 9.7 wt%. These high-concentration printing inks can provide better feasibility for the AM of nonporous all-aramid materials than the lower than 2 wt% ANF colloids used in other literature works [36,39,42]. Fig. S3 displays the viscosity of the six printing inks with respect to shear rate, where all inks exhibit a shear thinning behavior that is ideal for the precipitation printing process. After simultaneous precipitation printing and protonation of the ANF colloid into the PG bath (Fig. 1C), the printed wet ANF structures need to be washed and dried to form A-aramid structures.

The two drying processes in Fig. 1A can result in two A-aramid microstructures due to different drying mechanisms. During the thermal drying process, capillary force from water evaporation can induce ANF self-assembly, along with the hydrogen bonding and aromatic π-π stacking between the ANFs that can hierarchically order and pack ANFs. However, this self-assembly process causes significant dimensional contraction. In Fig. 2A, after drying a wet ANF cube (left), the obtained dense A-aramid structure (center) has 49 % dimensional contraction in the *x*-*y* plane (printing plane) and 62 % dimensional contraction in the *z*-direction (layer stacking direction) using the highest concentration Ink 6 (9.7 wt%). Higher dimensional contractions are observed when using a lower concentration printing ink (Table S2). After measuring the contraction in all three dimensions, larger wet structures can be designed to account for the predicted contraction and produce self-assembled structures with desired dimensions, and an example is demonstrated in Fig. 2A (right) to reproduce the geometry of the dense A-aramid cube. Here, the printed dimensions of the wet structure are 1.96 times the target value in both the *x*- and *y*-directions, and 2.63 times the target value in the *z*-direction. This drying process with proportional scaling has been proven effective for fully solid structures without internal holes, such as the propeller and gears shown in the later section, but also has limitations in building complex thin-wall structures due to contraction stability issues such as thin-wall buckling. As for the density, although the ANF printing ink concentration influences the contraction ratio during self-assembly, it does not have a significant effect ($p = 0.184$) on the final density of the dense A-aramid material (Fig. S4). The dense A-aramid material exhibits a density that is only 90 % of that of aramid fabric (1.44 g·cm^{-3}). This difference can be attributed to the reduced compactness of the macroscale A-aramid, which is self-assembled from branched ANFs, compared to industrial-grade wet-spun aramid fibers with their highly aligned aramid chains.

On the other hand, if freeze-drying is applied to a wet ANF cube (from Ink 6), the final contraction is below 5 % in all three dimensions (Fig. 2B), and the density of the porous A-aramid is only 0.123 g·cm^{-3} (91 % porosity). Furthermore, an ANF hollow nose cone structure is printed without the need for supporting material (Fig. 2C), and after freeze-drying it becomes a porous A-aramid structure that can be used as a lightweight, self-supporting thermal protection. It should be noted that due to the hollow design of this nose cone without internal support, the contraction in the height direction is more than the contraction in the radial direction.

For the sulfuric acid approach, the prepared aramid/H_2SO_4 liquid crystalline printing ink is extruded onto the printing substrate immersed in a water/PG mixture bath (Fig. 1D), which results in the precipitation of yellow aramid and the formation of wet aramid structures after printing. Due to the high viscosity of the aramid/H_2SO_4 printing ink, the precipitation rate of aramid in the sulfuric acid approach is significantly slower than the precipitation and protonation rate of ANFs in the ANF approach. Hence, the all-aramid material printing speed in the sulfuric approach is slower than the ANF approach. After printing, DI water washing and subsequent thermal drying, S-aramid 3D structures can be produced using this sulfuric acid approach, with considerable dimensional contractions shown in Fig. 2D. However, the contractions in this case (32 %–34 % in the *x*-*y* plane and 47 % in the *z* direction) are lower

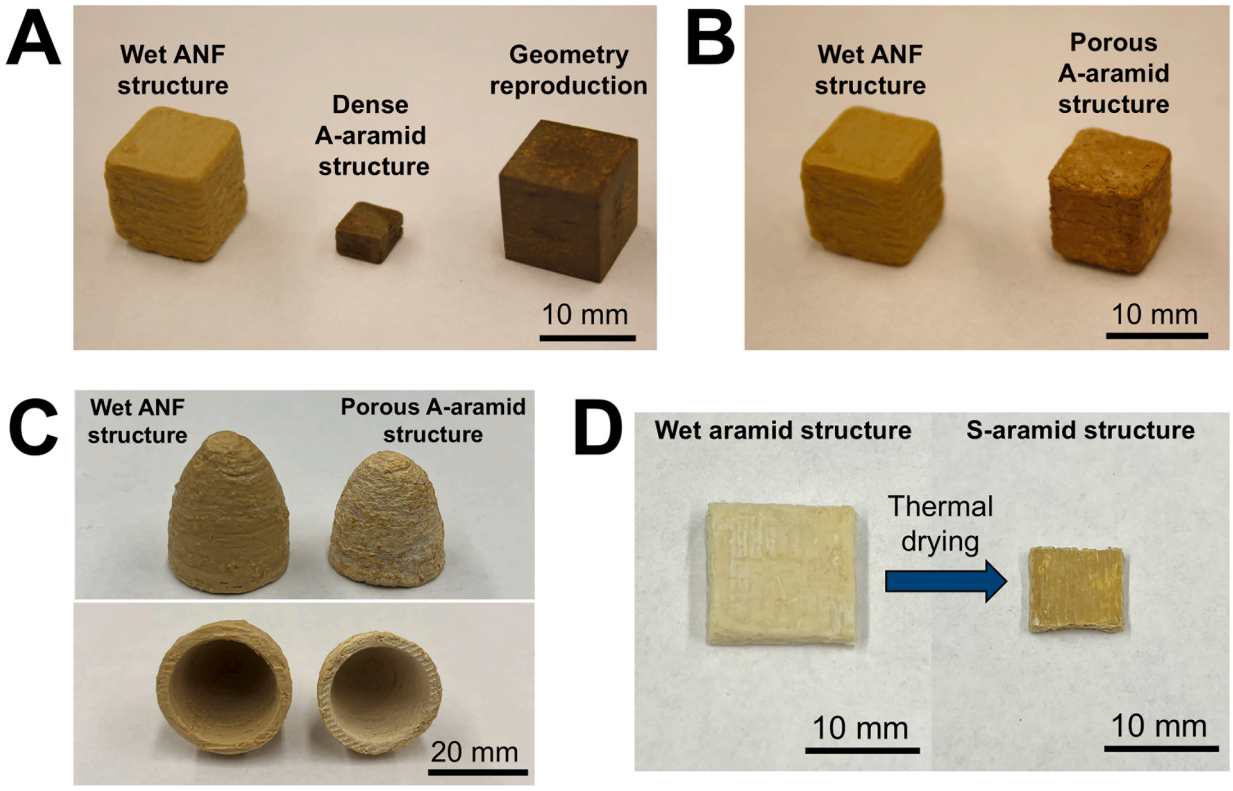

Fig. 2. A). Significant dimensional contraction after thermal drying and self-assembly through the ANF approach. B) Small dimensional contraction after freeze-drying through the ANF approach. C) Printed porous A-aramid nose cone before and after freeze-drying. D) Large dimensional contraction after thermal drying through the sulfuric acid approach.

than the dense A-aramid case when using a comparable printing ink concentration. The density of S-aramid is 0.843 ± 0.017 g·cm^{-3} (59 % of the density of aramid fabric), considerably lower than that of the dense A-aramid material. The lower density in this case is mainly attributed to the macroscale voids instead of a lower microstructure compactness. As can be seen in the cross-section SEM images shown in the next section, large voids are formed between the printing paths when precipitation printing the highly elastic liquid crystalline aramid/H_2SO_4 solution. Moreover, the requirement of concentrated H_2SO_4 poses a challenge for this lab-scale printing process, since typical stainless-steel and polypropylene nozzles and syringes do not have long-term resistance to concentrated H_2SO_4. Hence, this paper predominantly focuses on the ANF approach because of its superior printability and simpler handling, whereas S-aramid produced through the sulfuric acid approach serves solely for comparison purposes.

3.2. Characterization of printed All-Aramid materials

FTIR was first performed on the printed A-aramid, the printed S-aramid, and original aramid fabric. In Fig. 3A, all characteristic absorption peaks of the aramid fabric, including N-H stretching at 3315 cm^{-1}, C = O stretching at 1640 cm^{-1}, N-H bending and C-N stretching at 1538 cm^{-1}, and Ph-N vibration at 1304 cm^{-1} [33], are also shown in both spectra of A-aramid and S-aramid, indicating that the aramid chemical structure is preserved after printing. However, the wavenumbers of the N-H stretching, C = O stretching, and Ph-N vibration exhibit upshifts in the case of both A-aramid and S-aramid relative to the aramid fabric, implying a weaker overall hydrogen bonding effect between the aramid chains in printed all-aramid materials [51]. XRD (λ = 0.154 nm) was then performed to measure the crystallinity of the printed all-aramid materials. In Fig. 3B, A-aramid, S-aramid and aramid fabric all exhibit three diffraction peaks at $2\theta = 20.5°$ (110), 23° (200) and 28.4° (004). However, A-aramid shows a less intense (200) peak,

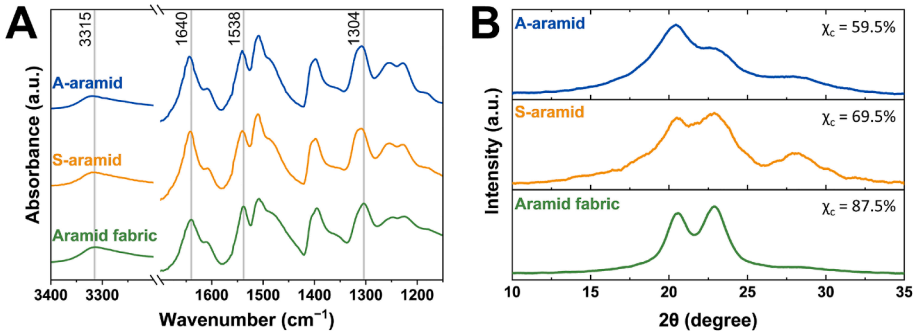

Fig. 3. A) FTIR spectra of the printed all-aramid materials compared to the aramid fabric. B) XRD patterns of printed all-aramid materials compared to the aramid fabric.

while S-aramid exhibits a more prominent (004) peak. This is because of the different aramid dissolution and reorganization mechanisms used in the ANF and sulfuric acid approaches that alter the orientation of the crystalline region. According to the curve deconvolution results in Fig. S5, the degree of crystallinity (χ_c) of the printed A-aramid and S-aramid are 59.5 % and 69.5 %, respectively, lower than that of the aramid fabric (87.5 %) due to the less order and alignment of the aramid chains after printing. Among the two printed all-aramid materials, the simple dissolution process through the sulfuric acid approach can preserve more crystallinity than the deprotonation process through the ANF approach.

Furthermore, the cross-section microstructure and morphology of the printed all-aramid structures were examined by SEM. The printed dense A-aramid structure has a compact cross-section without noticeable voids above micron-level (Fig. 4A), indicating the self-assembly and contraction process can automatically remove the defects produced between the printing paths. In addition, bundles of hierarchically assembled ANFs can be seen in the high magnification SEM image. In contrast, the porous A-aramid structure has a highly porous microstructure where ANFs are loosely interconnected to form a 3D network (Fig. 4B), and some macroscale defects can also be observed after the freeze-drying process. In the case of the S-aramid structure, a rough cross-section with macroscale defects formed between the printing paths is displayed in Fig. 4C, which implies that the precipitation printing process of the highly elastic liquid crystalline aramid/H_2SO_4 solution is not preferable for obtaining defect-free structures. However, high magnification SEM images of the relatively even and dense areas (red dashed rectangle) show that the microstructure of thermally dried S-aramid is still compact at micron-level, which is similar to the microstructure of thermally dried dense A-aramid.

3.3. Mechanical properties of printed All-Aramid materials

Aramid fibers are formed by a high-shear spinning process where stiff aramid chains are aligned with a high degree of hydrogen bonding and aromatic π-π interaction between parallel aramid chains, which leads to the high crystallinity and outstanding mechanical properties of the aramid fibers [50]. In this research, the goal is to maintain the mechanical properties of the 1D aramid fibers as closely as possible while producing 3D all-aramid structures through the proposed printing processes. Thus, the mechanical properties of the printed all-aramid materials were characterized through tensile testing (ASTM D638). The results of the printed dense A-aramid samples are displayed in Fig. 5A–5F. First, the tensile properties of the printed 0° infilled dense A-aramid samples produced from five different ANF printing inks (Ink 1–5) were studied. In Fig. 5A, both the Young's modulus and tensile strength of the dense A-aramid samples increase as the KOH/aramid ratio in the ANF printing ink decreases, while these mechanical properties do not show a clear trend with respect to the ANF printing ink concentration (Fig. S6). To explain the effect of KOH/aramid ratio, the diameter distributions of the protonated and isolated ANFs prepared from different printing inks are displayed in Fig. S7 and Fig. 5B, measured by AFM. As the KOH/aramid ratio reduces from 50 % to 32 %, the average diameter of the ANFs increases from 56 to 94 nm, indicating a lower degree of aramid deprotonation when using a low KOH/aramid ratio. Since a top-down then bottom-up ANF fabrication process is employed, maintaining a lower degree of deprotonation and a larger average diameter of the ANFs can better retain the mechanical properties of the original aramid fibers post-ANF reassembly, which elucidates the effect of KOH/aramid ratio. This trend is consistent with our previous work about self-assembled ANF films, where the modulus and strength of the ANF films improve as the KOH/aramid ratio reduces, but only when the

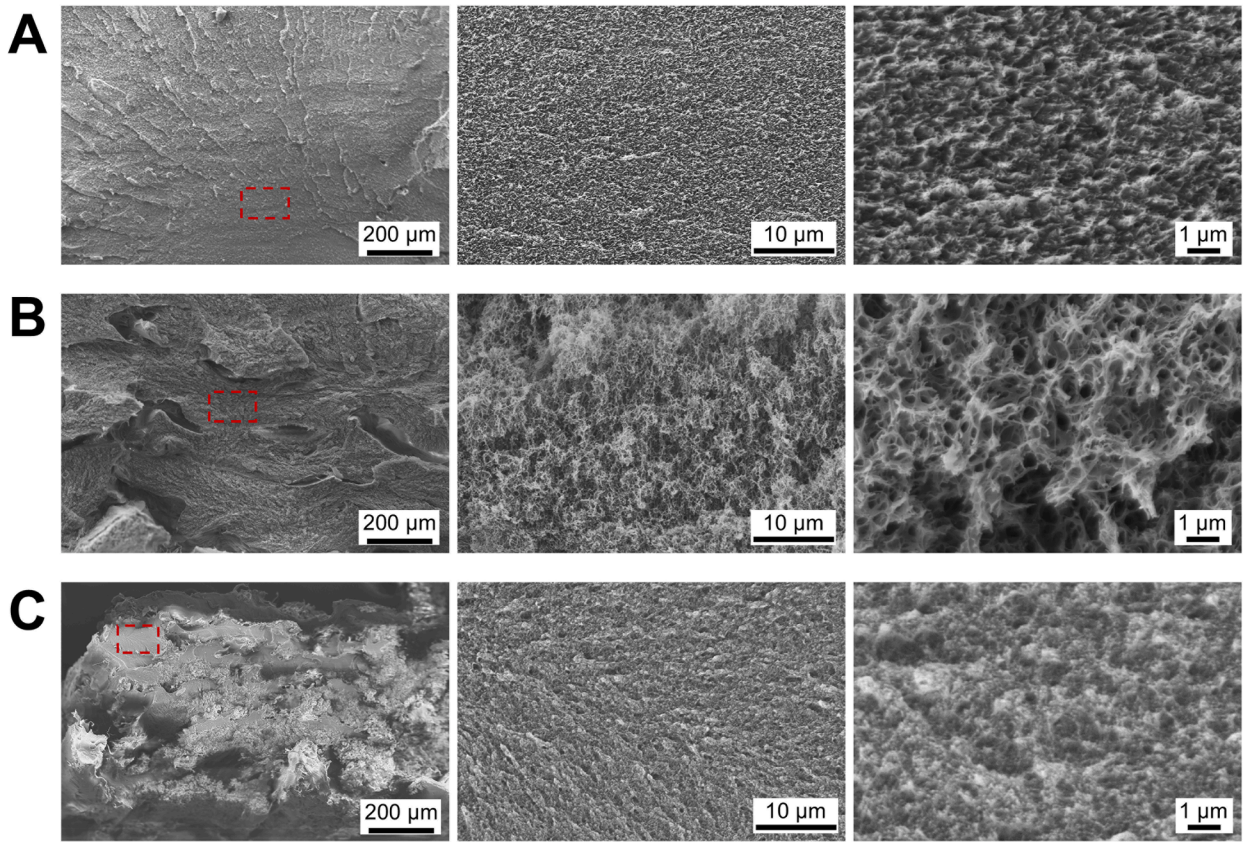

Fig. 4. A) Cross-section SEM images of a dense A-aramid structure. B) Cross-section SEM images of a porous A-aramid structure. C) Cross-section SEM images of an S-aramid structure. Red dashed rectangles in the first column indicate the zoomed-in areas. (For interpretation of the references to color in this figure legend, the reader is referred to the web version of this article.)

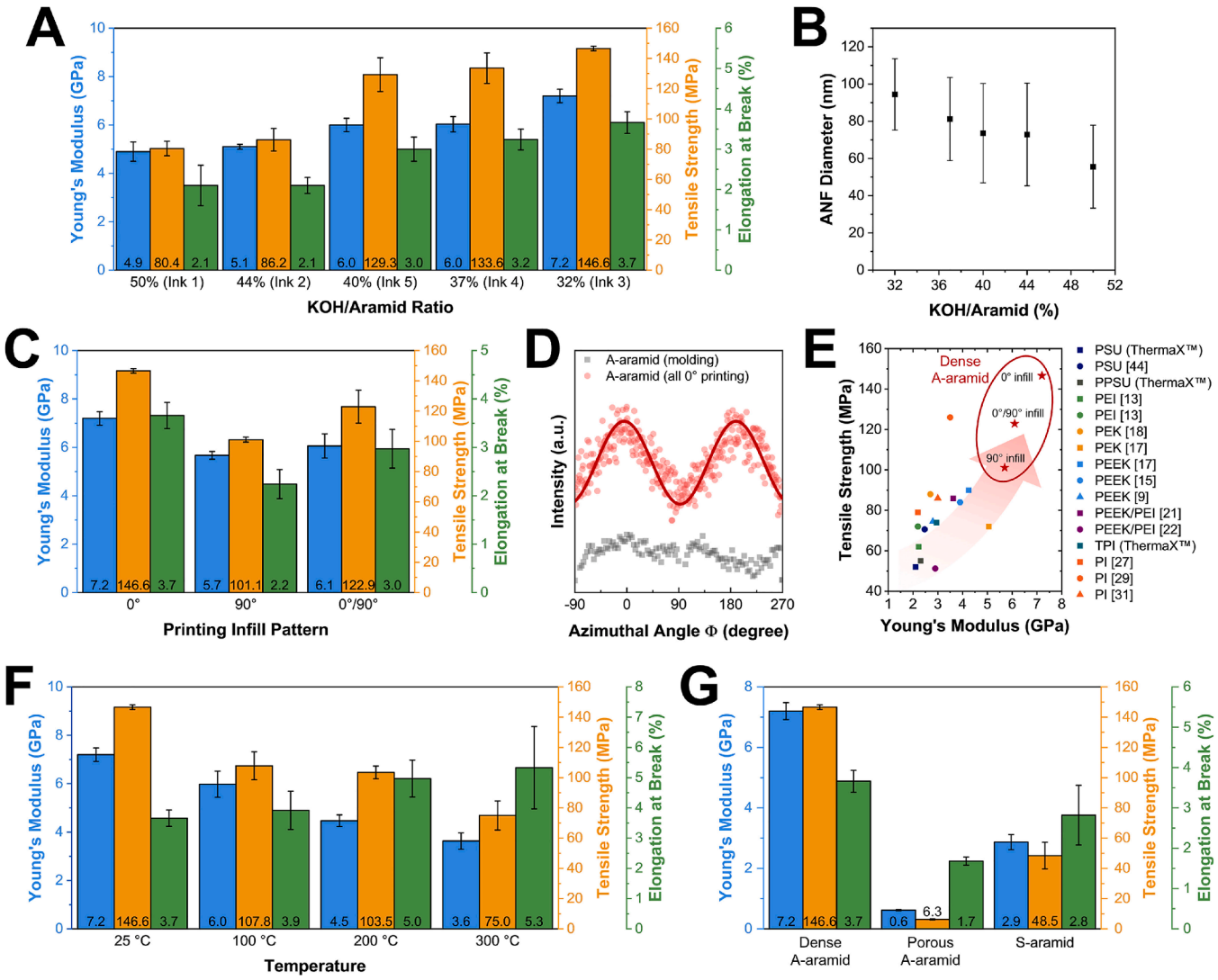

Fig. 5. A–F) Mechanical properties of the printed dense A-aramid: A) Effect of KOH/aramid ratio on the mechanical properties; B) Effect of KOH/aramid ratio on the ANF diameter; C) Effect of printing infill pattern on the mechanical properties; D) XRD azimuthal scans of the A-aramid materials; E) Comparison of the mechanical properties of the dense A-aramid to other unfilled, high-performance polymers produced by additive manufacturing; F) Effect of temperature on the mechanical properties. G) Mechanical properties comparison among the printed dense A-aramid, porous A-aramid and S-aramid.

KOH/aramid ratio is above a threshold to fully deprotonate aramid fibers and form homogeneous printing inks [38].

Moreover, the effect of printing infill patterns on the mechanical properties was tested based on the best-performance A-aramid group produced from Ink 3. In Fig. 5C, the printed dense A-aramid samples show significant anisotropy, where the 0° infilled (printing direction parallel to the loading direction) samples have the highest Young's modulus, tensile strength and elongation at break, the 0°/90° alternating infilled samples have intermediate properties, and the 90° infilled samples have the lowest properties. This anisotropy can be explained by the shear-induced alignment effect of high-aspect ratio ANFs during the printing process. The XRD azimuthal angle (Φ) scans at $2\theta = 20.5°$ (110) of the dense A-aramid materials produced by both molding and printing (0° infill) in Fig. 5D also confirm the crystalline region alignment effect through printing, which can be seen as two separate peaks with $\Delta\Phi = 180°$ apart. Furthermore, the mechanical properties of the dense A-aramid samples with the three different printing patterns are all remarkable, which include a Young's modulus up to 7.2 GPa and a tensile strength up to 146.6 MPa, significantly outperforming other unfilled (not fiber-reinforced), high-performance polymers produced by additive manufacturing processes such as material extrusion or powder bed fusion (Fig. 5E) [9,13,15,17,18,21,22,27,29,31,44]. In addition, the mechanical properties of the dense A-aramid samples (Ink 3, 0° infill) at elevated temperatures were measured to study their performance as high-temperature materials (Fig. 5F). The Young's modulus reduces from 7.2 to 3.6 GPa and the tensile strength decreases from 146.6 to 75.0 MPa when the service temperature increases from 25 to 300 °C, but the elongation at break increases from 3.7 % to 5.3 %. These changes in mechanical properties can be explained by the increased aramid chain mobility, weakened intermolecular bonds and reduced brittleness at elevated temperatures. The mechanical properties of the printed dense A-aramid at 300 °C are still comparable or even higher than the mechanical properties of various standard engineering polymers at room temperature, which implies the potential application of dense A-aramid as structural materials under extreme temperatures up to least 300 °C.

Finally, the mechanical properties of the printed porous A-aramid and the printed S-aramid samples are shown in Fig. 5G, which are compared to those of the dense A-aramid (0° infill). With a density only 9 % of the original aramid fabric, the porous A-aramid samples have a Young's modulus of 0.6 GPa and a tensile strength of 6.3 MPa, which are substantially lower than those of dense A-aramid. However, after considering the density, the specific modulus of porous A-aramid is only

11 % lower than the one of dense A-aramid, and the specific strength of porous A-aramid is about 55 % inferior to that of dense A-aramid (Fig. S8). In the case of S-aramid, since it has macroscale defects after drying (density only 59 % of the aramid fabric), its 2.9 GPa Young's modulus and 48.5 MPa tensile strength are also weaker than dense A-aramid, even if considering the specific properties (Fig. S8). In particular, the specific modulus of S-aramid is significantly lower than both dense and porous A-aramid. This is attributed to the nonuniform pore size in S-aramid, especially the presence of macroscale pores, which can amplify stress concentration and result in localized large strains under tensile loading. In contrast, a uniform pore distribution, as observed in porous A-aramid, can mitigate these effects on the specific modulus. Therefore, the ANF approach is a more promising process for precipitation printing of all-aramid materials, which allows for a defect-free, compact microstructure of dense A-aramid structures and excellent specific mechanical properties of porous A-aramid structures.

3.4. Thermal properties of printed All-Aramid materials

DMA was applied to the printed dense A-aramid and S-aramid samples from 30 to 500 °C in air. In the case of the dense A-aramid sample (Fig. 6A), its storage modulus drops to 3.35 GPa at 330 °C, half of the storage modulus at 30 °C, but remains stable in the range from 360 to 420 °C. This storage modulus reduction below 330 °C is caused by an increased chain mobility in the amorphous phase of dense A-aramid when temperature rises. The second drop of storage modulus above 420 °C is possibly related to the initial thermal decomposition such as the breakage of hydrogen bonds and π-π stacking interaction in the dense A-aramid sample. The small tan δ rises around 100°C and 200 °C correspond to the loss of moisture and the phase change of the trapped PG, respectively, while the tan δ peak at around 350 °C is related to the glass transition of the amorphous phase in dense A-aramid. As for the S-aramid sample, again, the evaporation of moisture and the phase change of a small amount of trapped PG can be observed on the tan δ curve (Fig. 6B). However, the glass transition behavior of S-aramid is weaker than dense A-aramid, due to the lower amount of amorphous phase in S-aramid according to XRD analysis. TGA was also performed on the printed all-aramid materials and the aramid fabric in a nitrogen environment, and the results are shown in Fig. 6C. The A-aramid sample has a T_d (5 % weight loss) of 517 °C, which is only 9 °C lower than the T_d of the S-aramid sample and 33 °C lower than that of the aramid fabric. The result implies that the deprotonation-reassembly process in the ANF approach reduces the overall degree of hydrogen bonding and π-π stacking interaction between the aramid backbones slightly more than the sulfuric acid approach. However, the printed all-aramid materials through both approaches inherit most of the high thermal stability of the aramid fabric.

In addition, since the printed dense A-aramid has remarkable short-term mechanical properties under high temperatures, its long-term mechanical properties under dynamic loading at 300 °C, 350 °C and 400 °C were tested through DMA. A dense A-aramid sample was subjected to a 2 N amplitude 1 Hz sinusoidal force (1.4 MPa stress amplitude) and kept isothermal at 300 °C and 350 °C for 1 day (86,400 cycles). The result in Fig. S9A shows that after the temperature reaches 300 °C, the storage modulus of dense A-aramid keeps increasing without any visible drop during this 1-day isothermal period. This stiffening phenomenon can be explained as improved aramid crystal alignment along the loading direction, especially under high temperatures when the aramid chain mobility is high. In the 350 °C test (Fig. S9B), the sample again exhibits an increasing trend of storage modulus with only a slight drop during the 1-day test. Nonetheless, no catastrophic sample failure occurs in this test. Finally, in Fig. S9C, when the temperature rises to 400 °C, the sample starts to show large damage after 6 h, and eventually breaks after 18 h. These long-term tests prove that the printed dense A-aramid can be continuously used as a structural material under extreme environmental conditions with temperatures up to 350 °C for over a day without catastrophic failure, but it can only withstand short-term dynamic loading at 400 °C. For future work, the effect of dynamic loading frequency and amplitude on the high-temperature strength of the printed all-aramid materials can be further investigated.

Since the aramid fabrics are famous as a flame-resistant material, the flame resistance of the printed all-aramid rectangular bars was also tested in this work. Fig. 6D shows the ignition tests of a printed dense A-aramid bar. After the first and second ignition by a butane torch, the dense A-aramid bar quickly stopped burning 0.3 s and 0.8 s after the flame was removed, respectively. After the third time ignition at the

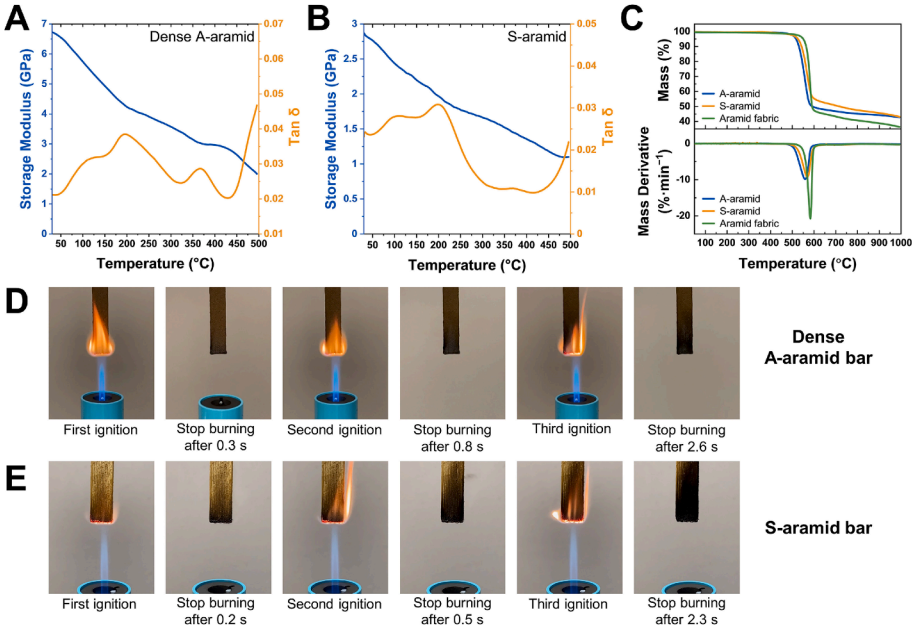

Fig. 6. A) Storage modulus and tan δ curves of a printed dense A-aramid sample. B) Storage modulus and tan δ curves of a printed S-aramid sample. C) TGA curves of the printed A-aramid and S-aramid, compared to the aramid fabric. D) Flame resistance test of a printed dense A-aramid bar. E) Flame resistance test of a printed S-aramid bar.

same tip location, the bar stopped burning 2.6 s after the removal of the flame. The same tests were also performed on a printed porous A-aramid bar in Fig. S10, which showed similar self-extinguishing results. As for the printed S-aramid bar in Fig. 6E, the self-extinguishing time is even shorter compared to the dense A-aramid case, indicating its better flame resistance due to higher thermal stability. Long-duration burning (30 s) tests in Video S1 show that the printed all-aramid bars can still self-extinguish within 30 s. These tests confirm the outstanding flame resistance of the printed all-aramid structures, which can be used in extreme environments to stop flames without any compromise of structural integrity.

3.5. Demonstration of printed All-Aramid 3D structures

Based on the mechanical and thermal characterization results, the printed dense A-aramid has outstanding performance compared to all existing unfilled, high-temperature polymers produced by AM. To further utilize its unprecedented performance and demonstrate its potential applications, several dense A-aramid 3D structures were printed using the highest concentration Ink 6. Fig. 7A shows a printed dense A-aramid gear set, whose gear teeth details are preserved without distortion after self-assembly and contraction. After drilling holes at their centers and inserting metal shafts, a high strength, high heat resistance and lightweight gear set is produced, which can potentially be used in high-temperature engines and gas turbines to replace metal gears. Fig. 7B displays a printed dense A-aramid propeller with a diameter of about 100 mm, similar to the size of a quad drone propeller. The A-aramid propeller is fixed on the shaft of a DC motor, which can spin in a hot environment created by a heat gun (Video S2). Thermal imaging using a FLIR ONE® PRO thermal camera shows that the propeller hub has a temperature of 227 °C and its blade has a temperature of 128 °C under heating. However, the A-aramid propeller has no shape distortion and shows no softening effect in this hot environment. Combining its excellent flame resistance shown in the previous section, the A-aramid materials can have potential applications in extreme environment exploration robots and fire rescue drones, where high-strength, heat-resistant and lightweight parts can be additively manufactured to replace traditionally machined metal parts.

4. Discussion

In this paper, two novel precipitation 3D printing processes for the fabrication of all-aramid structures are proposed and compared: the ANF approach and the sulfuric acid approach. As a comparison result, the ANF approach provides better printability, stronger mechanical properties of the final product, and higher printing efficiency, while the sulfuric acid approach is straightforward but it has handling difficulty and environmental issues due to the corrosive sulfuric acid. In addition, the ANF approach allows different microstructure porosities by using different drying methods, and local alignment of ANFs according to the printing path design. Thus, topology and fiber orientation optimization methods can be integrated in the design of printing paths for the A-aramid parts, to maximize structural performance for specific loading conditions. Considering all the factors, the ANF approach is more suitable for the development of industrial AM process of all-aramid structures. One key challenge regarding this process is the recycling of the coagulation bath, which means the purification process of PG to remove KOH and DMSO. Future research and development related to the recycling of coagulation bath to reduce waste and cost will largely promote the use of precipitation printing for industrial manufacturing of all-aramid structures.

As shown in Fig. 5E, the remarkable mechanical properties of the printed dense A-aramid can outperform other unfilled, high-performance thermoplastics and thermosets produced through AM. To offer a more comprehensive analysis, Fig. S11 presents a comparison chart of the mechanical properties of printed dense A-aramid and other high-performance materials produced through AM. The dense A-aramid provides a bridge between unfilled high-performance polymers and short fiber-reinforced polymer composites, while the tensile strength of the dense A-aramid even has advantage over most short fiber-reinforced polymer composites. Although the dense A-aramid has inferior Young's modulus and tensile strength to continuous fiber-reinforced polymer composites and alloys, it is still advantageous as a lightweight and homogeneous material. Moreover, the printed dense A-aramid has outstanding thermal stability compared to commercial high-performance thermoplastics such as polysulfone (Udel® P-3500) and polyamide imide (Torlon® 4000TF) in Fig. S12. With its combined advantages, the printed A-aramid is an excellent candidate for thermal and electrical insulation in jet engines, gas turbines, and transmissions, as well as for use as high-temperature fluid tubing.

5. Conclusions

In this work, AM of all-aramid structures is achieved through two precipitation 3D printing processes: the ANF approach and the sulfuric acid approach. In both approaches, the printing ink is extruded inside a non-solvent coagulation bath following the designed tool paths, while the solvent diffusion leads to the precipitation of aramid as a solid structure. After subsequent washing and drying, all-aramid 3D structures can be realized through both approaches. The comparison results

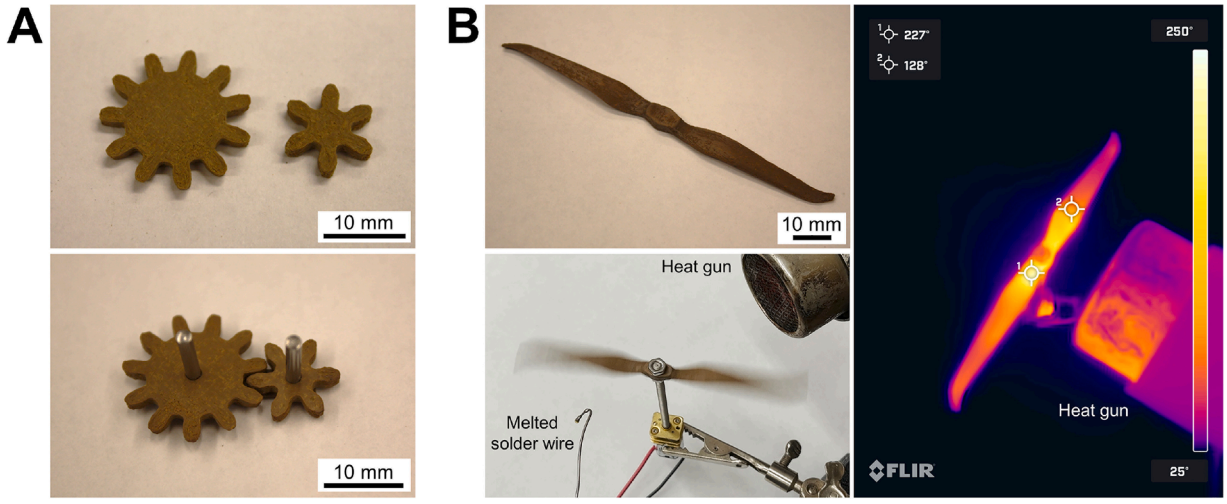

Fig. 7. A) A printed dense A-aramid gear set. B) A printed dense A-aramid propeller that can be used in a high-temperature environment.

show that the ANF approach surpasses the sulfuric acid approach due to its better printability, higher mechanical properties of the printed parts, and the ability for microstructure tailoring. The dense A-aramid structures after thermal drying and ANF self-assembly exhibit remarkable Young's modulus (up to 7.2 GPa) and tensile strength (up to 146.6 MPa), which exceed those of other unfilled, high-performance thermoplastics and thermosets produced through AM, both in literature and market. The printed porous A-aramid has low dimensional contractions after freeze drying while possessing a low density (0.123 $g{\cdot}cm^{-3}$) and an excellent specific modulus. Flame resistance tests, high-temperature mechanical tests and thermal analysis performed on the printed dense A-aramid samples also indicate that they are self-extinguishing and can be used in extreme environments with temperatures up to 350 °C. Finally, several complex dense A-aramid structures are printed to demonstrate the potential applications to fabricate lightweight, high-strength, heat-resistant polymeric structures as heat insulations, transmission parts and aircraft components to replace traditional metals or ceramics.

CRediT authorship contribution statement

Ruowen Tu: Writing – original draft, Validation, Methodology, Investigation, Formal analysis. **Hyun Chan Kim:** Writing – review & editing, Investigation, Funding acquisition, Formal analysis, Conceptualization. **Henry A. Sodano:** Writing – review & editing, Supervision, Resources, Funding acquisition, Conceptualization.

Declaration of competing interest

The authors declare the following financial interests/personal relationships which may be considered as potential competing interests: Ruowen Tu, Henry A. Sodano has patent #US11986993B2 issued to University of Michigan. If there are other authors, they declare that they have no known competing financial interests or personal relationships that could have appeared to influence the work reported in this paper.

Acknowledgements

We gratefully acknowledge support for this work from the National Science Foundation (US) under grant #EFRI-1935216, Air Force Office of Scientific Research through contract number FA9550-21-1-0019, and Army Research Office under contract number W911NF-18-1-0061. We also extend our gratitude to the support provided by the National Research Foundation of Korea (NRF) grant funded by the government of Republic of Korea (MSIT) under RS-2024-00353023. We want to thank Boyang Chen for performing the experiments of long-term dynamic mechanical analysis.

Appendix A. Supplementary data

Supplementary data to this article can be found online at https://doi.org/10.1016/j.matdes.2024.113547.

Data availability

Data will be made available on request.

References

[1] C.W. Weyhrich, T.E. Long, Additive manufacturing of high-performance engineering polymers: present and future, Polym. Int. 71 (2022) 532–536, https://doi.org/10.1002/pi.6343.
[2] P.M. Hergenrother, High performance polymer development, in: 1991. https://ntrs.nasa.gov/citations/19910013726 (accessed January 4, 2024).
[3] S.C. Ligon, R. Liska, J. Stampfl, M. Gurr, R. Mülhaupt, Polymers for 3D printing and customized additive manufacturing, Chem. Rev. 117 (2017) 10212–10290, https://doi.org/10.1021/acs.chemrev.7b00074.
[4] J.C. Vasco, Chapter 16 - Additive manufacturing for the automotive industry, in: J. Pou, A. Riveiro, J.P. Davim (Eds.), Additive Manufacturing, Elsevier, 2021: pp. 505–530. https://doi.org/10.1016/B978-0-12-818411-0.00010-0.
[5] M.J. El-Hibri, S.A. Weinberg, Polysulfones, in: Encyclopedia of Polymer Science and Technology, John Wiley & Sons, Ltd, 2001. https://doi.org/10.1002/0471440264.pst291.
[6] R.O. Johnson, H.S. Burlhis, Polyetherimide: A new high-performance thermoplastic resin, J. Polym. Sci. Polym. Symp. 70 (1983) 129–143, https://doi.org/10.1002/polc.5070700111.
[7] P. Chen, H. Wang, J. Su, Y. Tian, S. Wen, B. Su, C. Yang, B. Chen, K. Zhou, C. Yan, Y. Shi, Recent Advances on High-Performance Polyaryletherketone Materials for Additive Manufacturing, Adv. Mater. 34 (2022) 2200750, https://doi.org/10.1002/adma.202200750.
[8] M.Y. Keating, High glass transitions of high-performance thermoplastics, Thermochim. Acta 319 (1998) 201–212, https://doi.org/10.1016/S0040-6031(98)00419-5.
[9] K.M. Rahman, T. Letcher, R. Reese, Mechanical properties of additively manufactured PEEK components using fused filament fabrication, American Society of Mechanical Engineers Digital Collection (2016), https://doi.org/10.1115/IMECE2015-52209.
[10] W. Ye, G. Lin, W. Wu, P. Geng, X. Hu, Z. Gao, J. Zhao, Separated 3D printing of continuous carbon fiber reinforced thermoplastic polyimide, Compos. Part A Appl. Sci. Manuf. 121 (2019) 457–464, https://doi.org/10.1016/j.compositesa.2019.04.002.
[11] J.M. Gardner, G. Sauti, J.-W. Kim, R.J. Cano, R.A. Wincheski, C.J. Stelter, B. W. Grimsley, D.C. Working, E.J. Siochi, 3-D printing of multifunctional carbon nanotube yarn reinforced components, Addit. Manuf. 12 (2016) 38–44, https://doi.org/10.1016/j.addma.2016.06.008.
[12] W. Wu, Z. Li, G. Lin, J. Ma, Z. Gao, H. Qu, F. Zhang, Additive manufacturing of continuous BF-reinforced PES composite material and mechanical and wear properties evaluation, J. Mater. Sci. 57 (2022) 12903–12915, https://doi.org/10.1007/s10853-022-07425-z.
[13] K.C. Chuang, J.E. Grady, R.D. Draper, E.-S.E. Shin, C. Patterson, T.D. Santelle, Additive Manufacturing and Characterization of Ultem Polymers and Composites, in: Dallas, TX, 2015. https://ntrs.nasa.gov/citations/20160001352 (accessed February 23, 2023).
[14] J.-W. Tseng, C.-Y. Liu, Y.-K. Yen, J. Belkner, T. Bremicker, B.H. Liu, T.-J. Sun, A.-B. Wang, Screw extrusion-based additive manufacturing of PEEK, Mater. Des. 140 (2018) 209–221, https://doi.org/10.1016/j.matdes.2017.11.032.
[15] C. Yang, X. Tian, D. Li, Y. Cao, F. Zhao, C. Shi, Influence of thermal processing conditions in 3D printing on the crystallinity and mechanical properties of PEEK material, J. Mater. Process. Technol. 248 (2017) 1–7, https://doi.org/10.1016/j.jmatprotec.2017.04.027.
[16] B. Hu, X. Duan, Z. Xing, Z. Xu, C. Du, H. Zhou, R. Chen, B. Shan, Improved design of fused deposition modeling equipment for 3D printing of high-performance PEEK parts, Mech. Mater. 137 (2019) 103139, https://doi.org/10.1016/j.mechmat.2019.103139.
[17] N. Yi, R. Davies, A. Chaplin, O. Ghita, Novel backbone modified polyetheretherketone (PEEK) grades for powder bed fusion with enhanced elongation at break, Addit. Manuf. 55 (2022) 102857, https://doi.org/10.1016/j.addma.2022.102857.
[18] S. Berretta, Y. Wang, R. Davies, O.R. Ghita, Polymer viscosity, particle coalescence and mechanical performance in high-temperature laser sintering, J. Mater. Sci. 51 (2016) 4778–4794, https://doi.org/10.1007/s10853-016-9761-6.
[19] W. Ye, W. Wu, X. Hu, G. Lin, J. Guo, H. Qu, J. Zhao, 3D printing of carbon nanotubes reinforced thermoplastic polyimide composites with controllable mechanical and electrical performance, Compos. Sci. Technol. 182 (2019) 107671, https://doi.org/10.1016/j.compscitech.2019.05.028.
[20] G. Crevecoeur, G. Groeninckx, Binary blends of poly(ether ether ketone) and poly (ether imide): miscibility, crystallization behavior and semicrystalline morphology, Macromolecules 24 (1991) 1190–1195, https://doi.org/10.1021/ma00005a034.
[21] A. El Magri, S. Vaudreuil, Effects of physical and chemical ageing on 3D printed poly (ether ether ketone)/poly (ether imide) [PEEK/PEI] blend for aerospace applications, J. Mater. Sci. 58 (2023) 1465–1479, https://doi.org/10.1007/s10853-022-08068-w.
[22] Y. Abderrafai, A. Diouf-Lewis, F. Sosa-Rey, R.D. Farahani, N. Piccirelli, M. Lévesque, D. Therriault, Additive manufacturing and characterization of high temperature thermoplastic blends for potential aerospace applications, Compos. Sci. Technol. 231 (2023) 109839, https://doi.org/10.1016/j.compscitech.2022.109839.
[23] A. Yıldız, U. Emanetoğlu, E.O. Yenigun, H. Cebeci, Towards optimized carbon nanotubes (CNTs) reinforced polyetherimide (PEI) 3D printed structures: A comparative study on testing standards, Compos. Struct. 296 (2022) 115853, https://doi.org/10.1016/j.compstruct.2022.115853.
[24] M.F. Arif, H. Alhashmi, K.M. Varadarajan, J.H. Koo, A.J. Hart, S. Kumar, Multifunctional performance of carbon nanotubes and graphene nanoplatelets reinforced PEEK composites enabled via FFF additive manufacturing, Compos. B Eng. 184 (2020) 107625, https://doi.org/10.1016/j.compositesb.2019.107625.
[25] A. Diouf-Lewis, R.D. Farahani, F. Iervolino, J. Pierre, Y. Abderrafai, M. Lévesque, N. Piccirelli, D. Therriault, Design and characterization of carbon fiber-reinforced PEEK/PEI blends for Fused Filament Fabrication additive manufacturing, Mater. Today Commun. 31 (2022) 103445, https://doi.org/10.1016/j.mtcomm.2022.103445.
[26] Y. Chen, Z. Shan, X. Yang, Y. Song, A. Zou, Preparation of CCF/PEEK filaments together with property evaluation for additive manufacturing, Compos. Struct. 281 (2022) 114975, https://doi.org/10.1016/j.compstruct.2021.114975.

[27] M. Hegde, V. Meenakshisundaram, N. Chartrain, S. Sekhar, D. Tafti, C.B. Williams, T.E. Long, 3D Printing All-Aromatic Polyimides using Mask-Projection Stereolithography: Processing the Nonprocessable, Adv. Mater. 29 (2017) 1701240, https://doi.org/10.1002/adma.201701240.
[28] Y. Guo, J. Xu, C. Yan, Y. Chen, X. Zhang, X. Jia, Y. Liu, X. Wang, F. Zhou, Direct Ink Writing of High Performance Architectured Polyimides with Low Dimensional Shrinkage, Adv. Eng. Mater. 21 (2019) 1801314, https://doi.org/10.1002/adem.201801314.
[29] J. Zhang, Y. Zhang, L. Tao, T. Wang, Q. Wang, Integrated printing of high-strength, high-shape-retaining polyimide and its composite gradient structures for enhanced tribological properties, Addit. Manuf. 65 (2023) 103440, https://doi.org/10.1016/j.addma.2023.103440.
[30] Y. Guo, Z. Ji, Y. Zhang, X. Wang, F. Zhou, Solvent-free and photocurable polyimide inks for 3D printing, J. Mater. Chem. A 5 (2017) 16307–16314, https://doi.org/10.1039/C7TA01952A.
[31] A. Abbott, T. Gibson, G.P. Tandon, L. Hu, R. Avakian, J. Baur, H. Koerner, Melt extrusion and additive manufacturing of a thermosetting polyimide, Addit. Manuf. 37 (2021) 101636, https://doi.org/10.1016/j.addma.2020.101636.
[32] J.R. Brown, B.C. Ennis, Thermal Analysis of Nomex® and Kevlar® Fibers, Text. Res. J. 47 (1977) 62–66, https://doi.org/10.1177/004051757704700113.
[33] M. Yang, K. Cao, L. Sui, Y. Qi, J. Zhu, A. Waas, E.M. Arruda, J. Kieffer, M. D. Thouless, N.A. Kotov, Dispersions of Aramid Nanofibers: A New Nanoscale Building Block, ACS Nano 5 (2011) 6945–6954, https://doi.org/10.1021/nn2014003.
[34] B. Yang, L. Wang, M. Zhang, J. Luo, Z. Lu, X. Ding, Fabrication, Applications, and Prospects of Aramid Nanofiber, Adv. Funct. Mater. 30 (2020) 2000186, https://doi.org/10.1002/adfm.202000186.
[35] H.C. Kim, H.A. Sodano, Ultra-High Toughness Fibers Using Controlled Disorder of Assembled Aramid Nanofibers, Adv. Funct. Mater. 33 (2023) 2208661, https://doi.org/10.1002/adfm.202208661.
[36] P. Xia, H. Li, Y. Wang, J. Wang, Processing aramid nanofiber/modified graphene oxide hydrogel into ultrastrong nanocomposite film, Appl. Surf. Sci. 545 (2021) 149004, https://doi.org/10.1016/j.apsusc.2021.149004.
[37] Q. Yin, H. Jia, A. Mohamed, Q. Ji, L. Hong, Highly flexible and mechanically strong polyaniline nanostructure @ aramid nanofiber films for free-standing supercapacitor electrodes, Nanoscale 12 (2020) 5507–5520, https://doi.org/10.1039/C9NR09272B.
[38] R. Tu, H.C. Kim, O.A.H. Baabdullah, H.A. Sodano, Alignment Controlled Aramid Nanofiber-Assembled Films, Adv. Funct. Mater. 34 (2024) 2315422, https://doi.org/10.1002/adfm.202315422.
[39] G. Han, B. Zhou, Z. Li, Y. Feng, C. Liu, C. Shen, Ultrafine aramid nanofibers prepared by high-efficiency wet ball-milling-assisted deprotonation for high-performance nanopaper, Mater. Horiz. (2023), https://doi.org/10.1039/D3MH00600J.
[40] F. Zeng, X. Chen, G. Xiao, H. Li, S. Xia, J. Wang, A Bioinspired Ultratough Multifunctional Mica-Based Nanopaper with 3D Aramid Nanofiber Framework as an Electrical Insulating Material, ACS Nano 14 (2020) 611–619, https://doi.org/10.1021/acsnano.9b07192.
[41] J. Wang, X. Ma, J. Zhou, F. Du, C. Teng, Bioinspired, High-Strength, and Flexible MXene/Aramid Fiber for Electromagnetic Interference Shielding Papers with Joule Heating Performance, ACS Nano 16 (2022) 6700–6711, https://doi.org/10.1021/acsnano.2c01323.
[42] Q. Cheng, Y. Liu, J. Lyu, Q. Lu, X. Zhang, W. Song, 3D printing-directed auxetic Kevlar aerogel architectures with multiple functionalization options, J. Mater. Chem. A 8 (2020) 14243–14253, https://doi.org/10.1039/D0TA02590A.
[43] R. Tu, E. Sprague, H.A. Sodano, Precipitation printing towards diverse materials, mechanical tailoring and functional devices, Addit. Manuf. 35 (2020) 101358, https://doi.org/10.1016/j.addma.2020.101358.
[44] R. Tu, H.C. Kim, H.A. Sodano, Additive Manufacturing of High-Temperature Thermoplastic Polysulfone with Tailored Microstructure via Precipitation Printing, ACS Appl. Mater. Interfaces 15 (2023) 45270–45280, https://doi.org/10.1021/acsami.3c09048.
[45] R. Karyappa, A. Ohno, M. Hashimoto, Immersion precipitation 3D printing (*ip* 3DP), Mater. Horiz. 6 (2019) 1834–1844, https://doi.org/10.1039/C9MH00730J.
[46] H.-J. Chen, Q.-Y. Bai, M.-C. Liu, G. Wu, Y.-Z. Wang, Ultrafast, cost-effective and scaled-up recycling of aramid products into aramid nanofibers: mechanism, upcycling, closed-loop recycling, Green Chem. 23 (2021) 7646–7658, https://doi.org/10.1039/D1GC01805A.
[47] B. Yang, L. Wang, M. Zhang, J. Luo, X. Ding, Timesaving, High-Efficiency Approaches To Fabricate Aramid Nanofibers, ACS Nano 13 (2019) 7886–7897, https://doi.org/10.1021/acsnano.9b02258.
[48] Y. Zhao, Y. Qiu, Z. Mai, E. Ortega, J. Shen, C. Gao, B.V. der Bruggen, Symmetrically recombined nanofibers in a high-selectivity membrane for cation separation in high temperature and organic solvent, J. Mater. Chem. A 7 (2019) 20006–20012, https://doi.org/10.1039/C9TA07416C.
[49] S. Ifuku, H. Maeta, H. Izawa, M. Morimoto, H. Saimoto, Facile preparation of aramid nanofibers from Twaron fibers by a downsizing process, RSC Adv. 4 (2014) 40377–40380, https://doi.org/10.1039/C4RA06924B.
[50] E.G. Chatzi, J.L. Koenig, Morphology and Structure of Kevlar Fibers: A Review, Polym. Plast. Technol. Eng. 26 (1987) 229–270, https://doi.org/10.1080/03602558708071938.
[51] J. Zhu, M. Yang, A. Emre, J.H. Bahng, L. Xu, J. Yeom, B. Yeom, Y. Kim, K. Johnson, P. Green, N.A. Kotov, Branched Aramid Nanofibers, Angew. Chem. Int. Ed. Engl. 56 (2017) 11744–11748, https://doi.org/10.1002/anie.201703766.